Water-induced Diamond Formation at Earth's Core-Mantle Boundary

Byeongkwan Ko[1], Stella Chariton[2], Vitali B Prakapenka[2], Bin Chen[3], Edward J. Garnero[4], Mingming Li[4], and Sang-Heon Shim[5]

[1]Michigan State University
[2]University of Chicago
[3]University of Hawaii at Manoa
[4]Arizona State University
[5]ASU

November 23, 2022

Abstract

The carbon and water cycles in the Earth's interior are linked to key planetary processes, such as mantle melting, degassing, chemical differentiation, and advection. However, the role of water in the carbon exchange between the mantle and core is not well known. Here, we show experimental results of a reaction between Fe_3C and H_2O at pressures and temperatures of the deep mantle and core-mantle boundary (CMB). The reaction produces diamond, FeO, and FeH_x, suggesting that water can liberate carbon from the core in the form of diamond ("core carbon extraction") while the core gains hydrogen, if subducted water reaches to the CMB. Therefore, Earth's deep water and carbon cycles can be linked. The extracted core carbon can explain a significant amount of the present-day mantle carbon. Also, if diamond can be collected by mantle flow in the region, it can result in unusually high seismic-velocity structures.

Water-induced Diamond Formation at Earth's Core-Mantle Boundary

Byeongkwan Ko[1*], Stella Chariton[2], Vitali Prakapenka[2], Bin Chen[3], Edward J. Garnero[1], Mingming Li[1], Sang-Heon Shim[1]

[1]School of Earth and Space Exploration, Arizona State University, Tempe, AZ, USA
[2]Center for Advanced Radiation Sources, University of Chicago, Chicago, IL, USA
[3]Hawaii Institute of Geophysics and Planetology, University of Hawaii at Manoa, Honolulu, HI, USA

[*]Now at Department of Earth and Environmental Sciences, Michigan State University, East Lansing, MI, USA

Corresponding author: Byeongkwan Ko (kobyeong@msu.edu)

Key Points

- Water reacts with iron-carbon alloy to form diamond at the *P*–*T* conditions expected for Earth's core-mantle boundary.
- Some of Earth's mantle carbon may come from the core through water-induced reactions at the core-mantle boundary.
- Diamonds formed at the core-mantle boundary may result in high seismic velocity structures in the region.

Abstract

The carbon and water cycles in the Earth's interior are linked to key planetary processes, such as mantle melting, degassing, chemical differentiation, and advection. However, the role of water in the carbon exchange between the mantle and core is not well known. Here, we show experimental results of a reaction between Fe_3C and H_2O at pressures and temperatures of the deep mantle and core-mantle boundary (CMB). The reaction produces diamond, FeO, and FeH_x, suggesting that water can liberate carbon from the core in the form of diamond ("core carbon extraction") while the core gains hydrogen, if subducted water reaches to the CMB. Therefore, Earth's deep water and carbon cycles can be linked. The extracted core carbon can explain a significant amount of the present-day mantle carbon. Also, if diamond can be collected by mantle flow in the region, it can result in unusually high seismic-velocity structures.

Plain Language Summary

Carbon plays a vital role in geological processes occurring in the Earth's interior. While most carbon on Earth exists in its core, whether or not the core carbon can be added to the mantle is unclear due to the lack of knowledge of possible carbon transfer mechanism at the core-mantle boundary (CMB). We conducted experiments by reproducing the extreme pressure and temperature conditions of the CMB. Our experiments show that water can react with the metallic iron core and liberate carbon as diamond, suggesting an important relationship between Earth's water and carbon cycles on Earth. In addition, our result predicts possible existence of diamond in some regions of the deepest mantle.

1 Introduction

Distribution of carbon in its interior provides important clues for understanding the chemical evolution of the Earth. During the accretion processes, a vast majority of Earth's carbon could have been added to the core because of carbon's siderophile nature (Dasgupta et al., 2013; Fischer et al., 2020). The preferential partitioning of carbon into the metallic core predicts a very small amount of residual carbon in the silicate mantle after core formation (1–5 ppm; Dasgupta et al., 2013). However, the estimated carbon abundance in the present-day mantle is much greater (~120 ppm for pyrolite; McDonough and Sun, 1995). It remains unclear how the mantle has gained much more carbon (Dasgupta et al., 2013).

Several models for carbon replenishment to the mantle have been proposed to explain the present-day mantle inventory of carbon. For example, the additional carbon might have been delivered through a volatile-rich late veneer that occurred after core formation (Wänke, 1981). This model has difficulties explaining the difference in carbon isotopic composition between CI chondritic materials and the average mantle (Kerridge, 1985; Deines, 2002) and the superchondritic H/C ratio of the bulk silicate Earth in present day (Hirschmann and Dasgupta, 2009). Alternatively, carbon ingassing might have occurred after core formation. Carbon in an early atmosphere might have dissolved into an early magma ocean and precipitated graphite, diamond, or carbide, increasing the amount of the mantle carbon (Dasgupta et al., 2013). Also, some amount of carbon-bearing metallic melts might have been trapped in the mantle if incomplete segregation of metallic liquid from the mantle occurred during core formation (Dasgupta et al., 2013).

The core is the largest carbon reservoir within the Earth (McDonough, 2003), although estimates of the amount of carbon in the core vary, e.g., between 0.09–4 wt% (McDonough, 2003; Dasgupta and Walker, 2008; Wood et al., 2013; Dasgupta et al., 2013; Fischer et al., 2020). Therefore, core carbon loss to the mantle through CMB chemical reactions after core formation could be a viable source for the observed excess mantle carbon. Dasgupta et al. (2013) predicted that if deeply subducted hydrous minerals break down and release water at the CMB, water may react with the iron core. They further speculated that the reaction would form FeH_x and liberate carbon from the iron core by forming CO, CO_2, or $FeCO_3$. This hypothesis suggests that Earth's carbon, hydrogen, and water cycles may be linked at the CMB. Experiments have demonstrated the plausibility of hydrous minerals in subducting slabs, such as AlOOH (Piet et al., 2020), FeOOH (Nishi et al., 2017), phase H (Nishi et al., 2014), and hydrous SiO_2 (Lin et al., 2020; Nisr et al., 2020). Thus, subduction processes can result in the transport and release of water in the deepest mantle, although dehydration processes at the CMB could be more complicated than what has been observed in experiments on simplified chemical systems.

H, O, and C are all light element candidates for the core (e.g., Hirose et al., 2013), which could affect one another's solubility in the region. Experiments showed that $C_nH_{(2n+2)}$ paraffin reacts with Fe and forms Fe_3C, which was then replaced by FeH_x + diamond at 64 GPa and 1,650 K (Narygina et al., 2011) and up to 127 GPa and >2,100 K (Hirose et al., 2019). Hirose et al. (2019) also showed that the same reaction occurs even with liquid Fe at 58–66 GPa and 3,220–3,710 K. It thus appears that hydrogen's strong affinity to iron could lower the solubility of C in the core. However, whether iron carbide directly react with water to liberate carbon at pressure and temperature (*P*–*T*) conditions relevant to the CMB has never been tested by experiments. In order to understand the possibility of carbon exchange between the core and the mantle induced by the presence of water at the CMB, we conducted experiments on reactions between iron carbide (Fe_3C) and water (H_2O) at 70–140 GPa and up to 4,050 K (thus bracketing the CMB pressure of 136 GPa) using in-situ X-ray diffraction (XRD) in laser-heated diamond anvil cells (LHDACs). The experiments found formation of diamond from reaction between iron carbide and water, opening up a possibility for the chemical exchange between the core and the mantle.

2 Materials and Methods

Fe_3C was synthesized at high pressures using the multi-anvil press at the University of Hawaii at Manoa. The starting material was a mixture of Fe powder (99.9+% purity, Aldrich Chemical Company) and graphite powder (99.9995% purity, Alfa Aesar Company) with an atomic ratio Fe:C = 3:1. The mixture was loaded into a MgO capsule of an 18/12 multi-anvil cell assembly, which was then compressed to 3 GPa and heated at 1,300 K for 8 hours to synthesize Fe_3C. The Fe_3C sample was then analyzed by electron microprobe to confirm its purity and composition. The synthesized Fe_3C was loaded as ~10 μm-thick foils in the symmetric-type LHDACs with 150 and 200 μm-sized culets using a micro-manipulator (Microsupport Axis Pro SS) at Arizona State University (ASU). Distilled water was loaded as a pressure medium.

In-situ X-ray diffraction (XRD) experiments (Table 1) were conducted at sector 13-IDD of the GeoSoilEnviroConsortium (GSECARS) in the Advanced Photon Source (APS; Prakapenka et al., 2008). X-ray energy was 30 keV. The X-ray diffraction images were collected using a Dectris

Table 1: Experiment run table for in-situ X-ray diffraction experiments at high pressure (*P*) and temperature (*T*) conditions.

Sample #	*P* (GPa)	*T* (K)	Phase assemblage	V_{FeO} (Å^3)	$V_{diamond}$ (Å^3)
Sample #1[†]	71-74(8)	1,700-1,900	Fe_3C, FeO, d,f-FeH, C	62.68(4)	
Sample #2	92(8)	2,000	Fe_3C, FeO, d,f-FeH, C	59.58(1)	
	117(8)	2,200	Fe_3C, FeO, d,f-FeH, C	56.42(0)	
	127(8)	2,000	Fe_3C, FeO, d-FeH, C	55.62(1)	
Sample #3[‡]	120(8)	2,002	Fe_3C, FeO, d-FeH, C	55.96(1)	38.0(4)
	120(8)	1,998	Fe_3C, FeO, d-FeH, C	56.02(1)	38.0(4)
	125(13)	2,723	py, f-FeH, C, *		38.1(4)
	126(13)	2.758	py, f-FeH, C, *		38.0(4)
	133(13)	2,818	py, f-FeH, C, *		37.8(4)
	130(13)	2,970	py, f-FeH, C, *		38.0(4)
	131(13)	3,332	py, f-FeH, C, *		38.0(4)
	138(14)	3,862	py, f-FeH, C, *		37.9(4)
	140(14)	4,051	py, f-FeH, C, *		37.9(4)

Pressure was calculated based on unit-cell volume (*V*) of FeO (B1) or diamond by using their equation of state parameters (Fischer et al., 2011; Dewaele et al., 2008). Temperature uncertainties are estimated to be <200 K. d-FeH: dhcp-FeH_x, C: diamond, f-FeH: fcc-FeH_x, py: pyrite-type FeO_2H_x. *: X-ray diffraction lines which can be assigned to either dhcp-FeH_x or tetragonal FeH_2. [†]Pressure and temperature were maintained in the ranges throughout the sample. [‡] Temperature was increased at the same spot over the runs.

Pilatus detector and analyzed using DIOPTAS (Clemens et al., 2015) and PeakPo (Shim et al., 2017). The exposure time was 5–10 seconds. Typical X-ray and laser beam diameters were ~5 and

20 μm, respectively. The heating was conducted with a pre-set laser power which was directly applied at the start of the heating and maintained for 5 seconds each heating cycle. This heating method reduces the risk of overheating the diamond anvils particularly with water as a pressure medium, preventing LHDACs from failure during high-temperature heating. For temperature estimations, we fit the thermal radiation spectra measured from both sides of the sample to a Planck gray-body equation for estimation of temperature. The temperature uncertainty is estimated to be ~200 K considering the temperature reading difference between the two sides of the sample and the intrinsic uncertainty from the spectroradiometry.

At relatively low temperatures (<2,200 K), pressure was estimated using the equation of state (EOS) parameters of FeO in NaCl-type structure (Fischer et al., 2011). At higher temperatures (>2,700 K) for Sample #3 (Table 1), reliable pressures were difficult to estimate, unlike at the lower temperatures where robust diffraction lines of FeO are available. In this case, pressure was estimated from the EOS of diamond (Dewaele et al., 2008) based on its 111 peak position, which was identified more clearly than at lower temperatures. The calculations yield pressures up to 140 GPa (Table 1). The calculated pressures using the diamond at 2,000 K agree within 0.2–1.3% with those estimated using the NaCl-type FeO in the same heating spot in Sample #3. Given the fact that pressures of some runs are estimated from a single diffraction line, we assigned conservative uncertainty (10%) for the pressures at temperatures over 2,700 K. The samples could not be recovered to room conditions because of failure of diamond anvils during decompression or sample loss when H_2O converts to liquid during decompression to ∼1 bar.

Micro-Raman measurements were conducted for identifying diamond in Sample #1 at high pressures. A solid-state (frequency doubled Nd:YAG) laser was used with a 532 nm monochromatic beam at ASU. The laser power at the sample was ∼3 mW. The spectrometer was calibrated using the neon emission spectra. Measurements were conducted using an 1,800 grooves/mm grating. We calibrated pixel-to-pixel sensitivity differences in the charge-coupled device (CCD) detector using the spectrum of a glass with well-known fluorescence intensities at different wavenumbers. The exposure time for each spectrum measurement was 1–10 seconds. Pressure was determined using a diamond anvil Raman gauge (Akahama and Kawamura, 2006).

3 Results

XRD peaks of Fe_3C and ice X were confirmed at high pressures before laser heating. The diffraction peaks were broad because of differential stress. After laser heating of the samples, we found two sets of mineral assemblages depending on heating temperature. At lower temperatures of 1,700–2,200 K at 71–127 GPa (Samples #1 and 2; Table 1), we observed the diffraction peaks of FeO (NaCl-type, B1), dhcp-FeH_x, and possibly diamond (Fig. 1a and S1). Some XRD patterns show fcc-FeH_x as an additional phase with relatively weak peak intensities (Table 1). The diffraction peaks of Fe_3C were also observed as sharp peaks. The characteristic diffraction line of diamond 111 was difficult to separate from that of dhcp-FeH_x 004. A run at 120 GPa and 2,002 K showed a clear diamond peak at $2\theta \sim 16°$, which can be indexed as the 022 line (Fig. 1a).

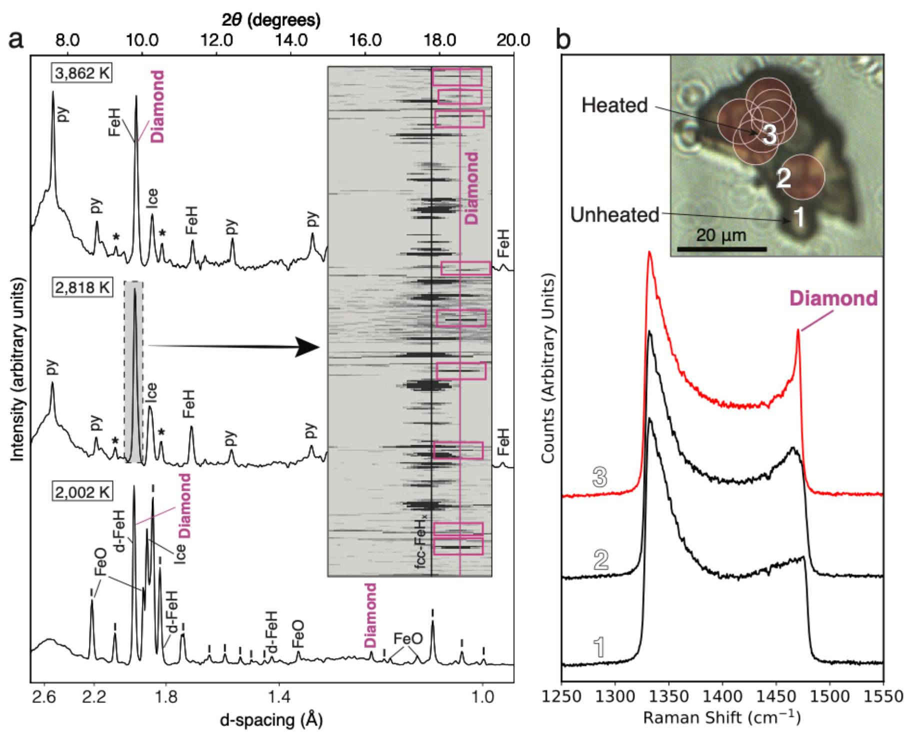

Figure 1: (a) In-situ X-ray diffraction (XRD) patterns of the sample at 120–138 GPa and 2,002–3,862 K in laser-heated diamond anvil cell. X-ray energy was 30 keV. The background is subtracted. Py: pyrite-type $FeOOH_x$; FeH: fcc-FeH_x; Ice: Ice X; d-FeH: dhcp-FeH_x. The black vertical ticks represent Fe_3C. The asterisks indicate a minor iron hydride phase (dhcp-FeH_x or FeH_2). The inset displays a 2-D diffraction image corresponding to the peak in the grey box for 2θ angles of (horizontal

axis) 9.5–10° and azimuth angles of 0–360° (vertical axis). The observed diamond 111 (the magenta rectangles) is clearly distinguished from the fcc-FeH$_x$ line. (b) High-pressure Raman spectra of the sample at 54.9 GPa and 300 K. The sample was synthesized at 60 GPa and 2,000 K. The semi-transparent red circles in the inset optical image represent heated areas. The locations of the measured spectra are numbered in the inset. The sharp peak of the red spectrum at 1470 cm^{-1} is from diamond crystals formed by the reaction between Fe_3C and H_2O in the heated part of the sample.

We further examined the sample synthesized at ∼72 GPa and ∼1,800 K in Raman spectroscopy (Sample #1; Table 1). In order to reduce the signal from the diamond anvils and enhance the signal from diamond formed from the reaction in the sample, we used the confocal micro-Raman technique which blocks out-of-focus light in signal detection. The strong peak at 1,320 cm^{-1} is from the uncompressed part of the diamond anvils (Fig. 1b). The right-hand side of the peak extends up to 1,470 cm^{-1}, which is from the compressed part of the diamond anvils. Because the diamond inside the sample is at a higher pressure than diamond anvil, the peak would appear at the end of the spectral feature (~1,470 cm^{-1}). The heated areas clearly showed a sharp peak at the edge of the spectral feature, whereas the unheated areas do not show such a peak (Fig. 1b), demonstrating the existence of diamond formed from the reaction between Fe_3C and H_2O. Raman spectra measured during decompression also showed the consistent results at 64, 55, 41, and 6 GPa (Fig. S2). At a temperature range of 1,700-2,200 K, the reaction can be summarized as:

$$\mathrm{Fe_3C + H_2O \rightarrow FeO + 2FeH\ (dhcp) + C\ (diamond)}.$$

At higher temperatures of 2,700–4,050 K (Sample #3), we observed the formation of pyrite-type FeOOH$_x$ (py-FeOOH$_x$), fcc-FeH$_x$, and diamond at 125–140 GPa (Fig. 1a). The diffraction lines of py-FeOOH$_x$ and fcc-FeH$_x$ are robustly observed. There are two unassigned diffraction peaks with weak intensities (labeled with "*" in Fig. 1a), which can be indexed with either dhcp-FeH$_x$ or FeH_2 (Fig. 1a). In either case, it is likely that the thermal gradient during laser heating promoted an appearance of additional iron hydride as a minor phase. At 3,860 K, the diffraction patterns remain similar to those measured at 2,720 K (Fig. 1a), but with stronger intensity in general, suggesting higher degree of reaction. The observation of diffraction lines for ice X is likely due to the axial thermal gradients as H_2O should be molten if excess H_2O exists (Schwager et al., 2004). Similarly, we infer that the diffraction lines of py-FeOOH$_x$ came from the cooler sample regions along the axial thermal gradients because its dehydration temperature is lower (Nishi et al., 2017) than the heating temperatures. We observed diffuse scattering in the diffraction patterns at temperatures over 2,700 K (Fig. S3) caused by melting. Temperatures greater than 2,700 K at 120–140 GPa are higher than the reported solidus of Fe_3C (Mashino et al. 2019), as well as the extrapolated solidus of FeH_x (Sakamaki et al., 2009). Therefore, the metallic melt should be rich in H at the heating center. Diamond should be stable under the studied *P–T* conditions because of its extremely high melting temperature (~7,000 K at 130 GPa; Wang et al., 2005) as observed in both XRD patterns and Raman spectra.

4 Discussion

4.1 Chemical Exchange Between the Mantle and Core

Previous experiments of paraffin + Fe metal showed that H is more siderophile than C, forming diamond at lower-mantle conditions (Narygina et al., 2011; Hirose et al., 2019), although it remains unclear that the reduced hydrogen can be provided to the lower mantle (Hu et al., 2016; Nishi et al., 2017). In our experiments of $Fe_3C + H_2O$, similar partitioning behaviors of H and C resulted in the formation of diamond. The formation of FeO and FeH_x observed in our experiments with excess water is consistent with previous experiments of $2Fe + H_2O = FeO + 2FeH$ with less water (6 wt% H_2O) at similar pressures and temperatures (~120 GPa and 2,000-2,250 K; Nishi et al., 2020). Also, the decomposition of H_2O at the CMB shown in this study agrees well with other experiments (Mao et al., 2017; Yuan et al., 2018).

This study demonstrates that not only water can play a critical role in chemical exchange between the mantle and the core, but also Earth's carbon cycle is closely linked to the H and O cycles. Our results found that at CMB conditions, metallic melt (rich in Fe and H) would form and most likely be incorporated into the liquid outer core (Fig. 2a). Some amount of O would remain in the mantle as iron oxide (FeO), while the metallic melt may also carry O to the core.

The water release from the dehydration of hydrous minerals in subducting slabs may have been a continuous process from when the hydrated slabs first reached the CMB following the initiation of plate tectonics. Although the timing of the onset of subduction is not well constrained, studies indicate that subduction might have initiated 2.5–3.5 Ga (Laurent et al., 2014; Tang et al., 2016;

Condie and Kröner, 2008). Theoretical and experimental studies have suggested that subducting slabs would have been negatively buoyant in the transition zone and the topmost lower mantle since subduction initiated, thus promoting their descent to the deep lower mantle (Klein et al., 2017; Ko et al., 2020). If water in subducting slabs has been transported to the CMB and released in the region for ~3 billion years, the core-mantle chemical exchange presented here may have occurred during the time.

The carbon transfer from the core to the mantle results in the gradual augmentation of the mantle carbon for a significant portion of the Earth's history. This is consistent with the earlier hypothesis that water may facilitate carbon transfer at the CMB by Dasgupta et al. (2013), which may

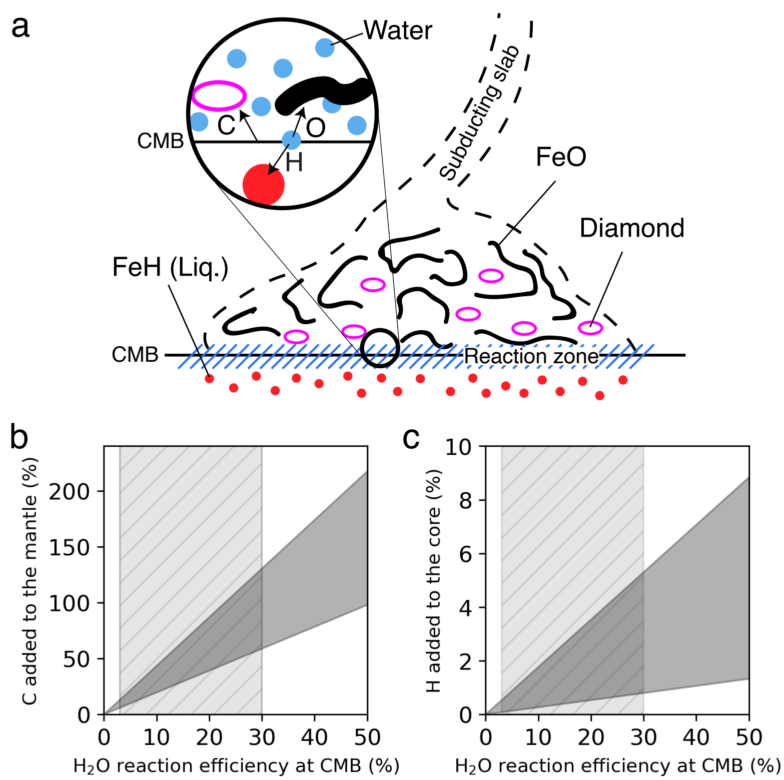

Figure 2: (a) Schematic diagram of the core-mantle boundary (CMB) region. Water (blue droplets in the inset) released from dehydration of a subducted slab causes a chemical reaction with liquid iron core in a reaction zone (blue shade) at the CMB. Diamond (magenta circles) and FeO (black lines) could be incorporated into the mantle, while hydrogen (red dots) could alloy with iron metal in the outer core. (b) The amount of carbon extracted from the core to the mantle for 3 Ga relative to the carbon content in the present-day mantle (120 ppm C; Mcdonough and Sun, 1995). (c) The

amount of hydrogen added to the core for 3 Ga relative to the hydrogen content in the present-day outer core (0.3–2.0 wt%; Terasaki et al., 2012; Umemoto and Hirose, 2015; Thompson et al., 2018; Tagawa et al., 2021). (b, c) H_2O reaction efficiency at the CMB represents the water amount reacting with the core at the CMB divided by the water amount subducted at the surface (Cai et al., 2018; see Supplementary information for detail). The hatched area represents the 3-30% of the reaction efficiency.

account for the present-day mantle carbon content (e.g., 120 ppm C; McDonough and Sun, 1995). However, the form of carbon produced from the CMB reaction in the present study is diamond, different from the oxidized carbon assumed by Dasgupta et al.

The amount of core carbon added to the mantle by the water-induced reaction at the CMB (after core formation) can be estimated. Efficiency of the reaction was defined as the water amount participating in the reaction at the CMB divided by the water amount subducted at the Earth's surface (see Supplementary information for detail). It should be noted that how much subducted water reaches the CMB is poorly constrained because of large uncertainties in dehydration and re-hydration processes in the mantle (Walter, 2021). In this estimation, a constant rate of water transport was assumed via subduction from the surface (3×10^{12} kg/yr H_2O for the global water flux at the surface in present day; Cai et al., 2018) for 3 Ga. Also, we assumed a constant carbon content in the outer core (0.9–2.0 wt%; Nakajima et al., 2015; Li et al., 2019). If 3–30% of subducted water reaches the CMB and reacts with the core (see Supplementary Information for detail), 7–160 ppm C can be added to the mantle over 3 Ga after core formation.

The proposed model thus has the potential to account for a substantial portion of the present-day carbon in the mantle. For example, 120 ppm of the present-day carbon content (McDonough and Sun, 1995) can be explained solely by the water-induced carbon transfer from the core (Fig. 2b), if water has been efficiently transported to the CMB over the last 3 Ga. Yet, this calculated "core carbon extraction" is only 0.2–1.7% (0.3–6.3 x 10^{20} kg C) of the estimated carbon content of the present-day outer core (Nakajima et al., 2015; Li et al., 2019). Therefore, most of the core carbon incorporated during its formation would still remain there. In addition, the model can estimate the amount of hydrogen added to the core through the water-induced reaction. If hydrogen alloys with iron metal with a 1:1 molar ratio (Supplementary Information), for the above assumed water transport efficiency for the core carbon extraction, our calculation predicts that the amount of hydrogen added to the outer core (0.3–3.0 x 10^{20} kg H) accounts for only 0.1–5.3% of the estimated present-day core hydrogen (Terasaki et al., 2012; Umemoto and Hirose, 2015; Thompson et al., 2018; Tagawa et al., 2021; Fig. 2c). Therefore, the core's carbon and hydrogen budgets would not be altered significantly by the core carbon extraction and are mainly determined during core formation.

4.2 Seismic implications

Diamond formed at the CMB is expected to be advected by mantle flow, ultimately entrained by upwelling mantle currents. This process is facilitated by the anomalously low density of diamond (32% lower than the surrounding mantle). Therefore, diamond residency at the CMB may be limited, but small-scale convection on the CMB may lead to temporary localized accumulations of diamonds even in regions strongly affected by subducted slabs in the lowermost mantle (Solomatov and Moresi, 2002; Li, 2020). Thus, regions with diamonds may not be ubiquitous at the CMB, but we expect their presence in CMB regions of deeply subducting hydrated slabs.

A question pertains whether the lowermost mantle diamond can be advected by upwelling mantle to the uppermost mantle. Diamond may react with metallic iron in the lower mantle to form iron carbide during ascent, but diamond can coexist with Fe_7C_3 if the carbon proportion is over 8 wt% (Lord et al., 2009). The upwelling flow would undergo an inevitable redox change when passing the 660-km discontinuity where Fe^{3+}-rich bridgmanite is destabilized and diamond is oxidized to carbonatite melts (Rohrbach and Schmidt, 2011). Such a redox change would make the upwelling of the lowermost mantle diamond to the uppermost mantle difficult. However, the carbonatite melt can still carry information about other minerals entrained together with the diamond from the CMB. If the melt crystallizes new diamond that is sent to the surface, diamond inclusions can exhibit geochemical signatures of their deep origin. Some diamond inclusions show low Mg# (0.2–0.6) in magnesiowüstite (Harte and Hudson, 2013; Hayman, et al., 2005; Kaminsky et al., 2009; Wirth et al., 2014) and an association of iron carbide and diamond (Kaminsky and Wirth, 2011), suggesting the possibility of their deep origin at the CMB, as advocated in this study.

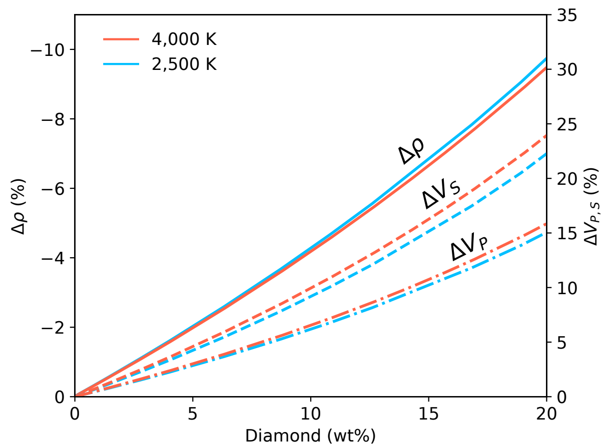

Figure 3: Density (solid lines), compressional (dotdashed lines), and shear wave velocities (dashed lines) of diamond + pyrolite with respect to pure pyrolite at the core-mantle boundary conditions (136 GPa). The red and blue lines were calculated for 4,000 and 2,500 K, respectively.

Diamond exhibits higher bulk and shear moduli as well as lower density compared to major mantle minerals (Valdez et al., 2012), and therefore 50–72% and 74–110% higher P (V_P) and S wave velocities (V_S), respectively, than pyrolite in the lower mantle. We calculated the V_S and density for the mineral assemblage of pyrolite + diamond with varying diamond proportion (0–20 wt%) at the CMB conditions (136 GPa and 2,500–4,000 K) using the Perple_X thermodynamic modeling program (Connolly, 2009) with the SBL2011 dataset (Stixrude and Lithgow-Bertelloni, 2011) and seismic properties of diamond (Dewaele et al., 2008; Valdez et al., 2012). The calculation demonstrates that even a small amount of diamond mixed with the background mantle can dramatically decrease density and increase V_P and V_S at the CMB (Fig. 3). Therefore, if diamond-bearing structures exist at the CMB, their exceptionally fast velocities could be detectable in seismic studies. Considering the fact that less dense structures could have longer resident time in regions with strong downgoing flow, the high velocity structures could be found regions associated with subducting slabs in the lowermost mantle.

5. Conclusions

We conducted experiments on reaction between Fe_3C and H_2O using LHDACs combined with in-situ X-ray diffraction at 70–140 GPa and up to 4,050 K. We found that the reaction liberates carbon in the form of diamond as hydrogen and oxygen alloy with iron. This result implies that the Earth's core carbon may have been transferred to the mantle if subducted water has reacted with the core. Our model provides a testable prediction that such diamonds, if locally collected by mantle flow, lead to small-scale high velocity structures near the subducted materials at the CMB.

Acknowledgments

This work has been supported by National Science Foundation (NSF) EAR-CSEDI-1401270 and EAR-1921298 and the National Aeronautics and Space Administration (NASA) Exoplanet 80NSSC18K0353. B. Chen acknowledges the support from NSF grants EAR-1555388 and EAR-2127807. This research used resources of the Advanced Photon Source (APS), a U.S. Department of Energy (DOE) Office of Science User Facility operated for the DOE Office of Science by Argonne National Laboratory under Contract No. DE-AC02-06CH11357. We acknowledge the support of GeoSoilEnviroCARS (Sector 13), which is supported by the National Science Foundation (NSF) - Earth Sciences (EAR-1634415), and the Department of Energy, Geosciences (DE-FG02-94ER14466).

Data Availability Statement

Datasets for this research are available online (https://doi.org/10.5281/zenodo.6040059).

References

Akahama, Y., & Kawamura, H. (2006). Pressure calibration of diamond anvil Raman gauge to 310 GPa. *Journal of Applied Physics*, 100(4), 043516.

Cai, C., Wiens, D. A., Shen, W., & Eimer, M. (2018). Water input into the Mariana subduction zone estimated from ocean-bottom seismic data. *Nature*, 563(7731), 389-392.

Condie, K. C., & Kröner, A. (2008). When did plate tectonics begin?: Evidence from the geologic record. *Geological Society of America Special Papers, 440*, 281-294.

Connolly, J. A. D. (2009). The geodynamic equation of state: what and how. *Geochemistry, Geophysics, Geosystems*, *10*(10).

Dasgupta, R., & Walker, D. (2008). Carbon solubility in core melts in a shallow magma ocean environment and distribution of carbon between the Earth's core and the mantle. *Geochimica et Cosmochimica Acta*, *72*(18), 4627-4641.

Dasgupta, R., Chi, H., Shimizu, N., Buono, A. S., & Walker, D. (2013). Carbon solution and partitioning between metallic and silicate melts in a shallow magma ocean: Implications for the origin and distribution of terrestrial carbon. *Geochimica et Cosmochimica Acta*, *102*, 191-212.

Deines, P. (2002). The carbon isotope geochemistry of mantle xenoliths. *Earth-Science Reviews*, 58(3-4), 247-278.

Dewaele, A., Datchi, F., Loubeyre, P., & Mezouar, M. (2008). High pressure–high temperature equations of state of neon and diamond. *Physical Review B*, 77(9), 094106.

Fischer, R. A., Campbell, A. J., Shofner, G. A., Lord, O. T., Dera, P., & Prakapenka, V. B. (2011). Equation of state and phase diagram of FeO. *Earth and Planetary Science Letters*, *304*(3-4), 496-502.

Fischer, R. A., Cottrell, E., Hauri, E., Lee, K. K., & Le Voyer, M. (2020). The carbon content of Earth and its core. *Proceedings of the National Academy of Sciences*, *117*(16), 8743-8749.

Harte, B. (2010). Diamond formation in the deep mantle: the record of mineral inclusions and their distribution in relation to mantle dehydration zones. *Mineralogical Magazine*, *74*(2), 189-215.

Harte, B., & Hudson, N. F. (2013). Mineral associations in diamonds from the lowermost upper mantle and uppermost lower mantle. In *Proceedings of 10th International Kimberlite Conference*, New Delhi (pp. 235-253). Springer.

Hayman, P. C., Kopylova, M. G., & Kaminsky, F. V. (2005). Lower mantle diamonds from Rio Soriso (Juina area, Mato Grosso, Brazil). *Contributions to Mineralogy and Petrology*, *149*(4), 430-445.

Hirose, K., Labrosse, S., & Hernlund, J. (2013). Composition and state of the core. *Annual Review of Earth and Planetary Sciences*, *41*, 657-691.

Hirose, K., Tagawa, S., Kuwayama, Y., Sinmyo, R., Morard, G., Ohishi, Y., & Genda, H. (2019). Hydrogen limits carbon in liquid iron. *Geophysical Research Letters*, 46(10), 5190-5197.

Hirschmann, M. M., & Dasgupta, R. (2009). The H/C ratios of Earth's near-surface and deep reservoirs, and consequences for deep Earth volatile cycles. *Chemical Geology*, *262*(1-2), 4-16.

Hu, Q., Kim, D. Y., Yang, W., Yang, L., Meng, Y., Zhang, L., & Mao, H. K. (2016). FeO_2 and FeOOH under deep lower-mantle conditions and Earth’s oxygen–hydrogen cycles. *Nature*, *534*(7606), 241-244.

Kaminsky, F. V., Khachatryan, G. K., Andreazza, P., Araujo, D., & Griffin, W. L. (2009). Super-deep diamonds from kimberlites in the Juina area, Mato Grosso State, Brazil. *Lithos*, *112*, 833-842.

Kaminsky, F. V., & Wirth, R. (2011). Iron carbide inclusions in lower-mantle diamond from Juina, Brazil. *The Canadian Mineralogist*, *49*(2), 555-572.

Kaminsky, F. (2012). Mineralogy of the lower mantle: A review of ‘super-deep’mineral inclusions in diamond. *Earth-Science Reviews*, *110*(1-4), 127-147.

Kerridge, J. F. (1985). Carbon, hydrogen and nitrogen in carbonaceous chondrites: Abundances and isotopic compositions in bulk samples. *Geochimica et Cosmochimica Acta*, *49*(8), 1707-1714.

Klein, B. Z., Jagoutz, O., & Behn, M. D. (2017). Archean crustal compositions promote full mantle convection. *Earth and Planetary Science Letters*, *474*, 516-526.

Ko, B., Prakapenka, V., Kunz, M., Prescher, C., Leinenweber, K., & Shim, S. H. (2020). Mineralogy and density of Archean volcanic crust in the mantle transition zone. *Physics of the Earth and Planetary Interiors*, *305*, 106490.

Laurent, O., Martin, H., Moyen, J. F., & Doucelance, R. (2014). The diversity and evolution of late-Archean granitoids: Evidence for the onset of "modern-style" plate tectonics between 3.0 and 2.5 Ga. *Lithos*, *205*, 208-235.

Li, M. (2020). The formation of hot thermal anomalies in cold subduction-influenced regions of Earth's lowermost mantle. *Journal of Geophysical Research: Solid Earth*, *125*(6), e2019JB019312.

Li, Y., Vočadlo, L., Alfè, D., & Brodholt, J. (2019). Carbon partitioning between the Earth's inner and outer core. *Journal of Geophysical Research: Solid Earth*, *124*(12), 12812-12824.

Lin, Y., Hu, Q., Meng, Y., Walter, M., & Mao, H. K. (2020). Evidence for the stability of ultrahydrous stishovite in Earth's lower mantle. *Proceedings of the National Academy of Sciences*, *117*(1), 184-189.

Lord, O. T., Walter, M. J., Dasgupta, R., Walker, D., & Clark, S. M. (2009). Melting in the Fe–C system to 70 GPa. *Earth and Planetary Science Letters*, *284*(1-2), 157-167.

Mao, H. K., Hu, Q., Yang, L., Liu, J., Kim, D. Y., Meng, Y., ... & Mao, W. L. (2017). When water meets iron at Earth's core–mantle boundary. *National Science Review*, *4*(6), 870-878.

Mashino, I., Miozzi, F., Hirose, K., Morard, G., & Sinmyo, R. (2019). Melting experiments on the Fe–C binary system up to 255 GPa: Constraints on the carbon content in the Earth's core. *Earth and Planetary Science Letters*, *515*, 135-144.

McDonough, W. F., & Sun, S. S. (1995). The composition of the Earth. *Chemical geology*, *120*(3-4), 223-253.

McDonough, W. F. (2003). 3.16–Compositional model for the Earth's core. *Treatise on geochemistry*, *2*, 547-568.

Nakajima, Y., Imada, S., Hirose, K., Komabayashi, T., Ozawa, H., Tateno, S., ... & Baron, A. Q. (2015). Carbon-depleted outer core revealed by sound velocity measurements of liquid iron–carbon alloy. *Nature communications*, *6*(1), 1-7.

Narygina, O., Dubrovinsky, L. S., McCammon, C. A., Kurnosov, A., Kantor, I. Y., Prakapenka, V. B., & Dubrovinskaia, N. A. (2011). X-ray diffraction and Mössbauer spectroscopy study of fcc iron hydride FeH at high pressures and implications for the composition of the Earth's core. *Earth and Planetary Science Letters*, *307*(3-4), 409-414.

Nishi, M., Irifune, T., Tsuchiya, J., Tange, Y., Nishihara, Y., Fujino, K., & Higo, Y. (2014). Stability of hydrous silicate at high pressures and water transport to the deep lower mantle. *Nature Geoscience*, *7*(3), 224-227.

Nishi, M., Kuwayama, Y., Tsuchiya, J., & Tsuchiya, T. (2017). The pyrite-type high-pressure form of FeOOH. *Nature*, *547*(7662), 205-208.

Nishi, M., Kuwayama, Y., Hatakeyama, T., Kawaguchi, S., Hirao, N., Ohishi, Y., & Irifune, T. (2020). Chemical Reaction Between Metallic Iron and a Limited Water Supply Under Pressure: Implications for Water Behavior at the Core-Mantle Boundary. *Geophysical Research Letters*, *47*(19), e2020GL089616.

Nisr, C., Chen, H., Leinenweber, K., Chizmeshya, A., Prakapenka, V. B., Prescher, C., ... & Shim, S. H. (2020). Large H_2O solubility in dense silica and its implications for the interiors of water-rich planets. *Proceedings of the National Academy of Sciences*, *117*(18), 9747-9754.

Núñez Valdez, M., Umemoto, K., & Wentzcovitch, R. M. (2012). Elasticity of diamond at high pressures and temperatures. *Applied Physics Letters*, *101*(17), 171902.

Piet, H., Leinenweber, K. D., Tappan, J., Greenberg, E., Prakapenka, V. B., Buseck, P. R., & Shim, S. H. (2020). Dehydration of δ-AlOOH in Earth's Deep Lower Mantle. *Minerals*, *10*(4), 384.

Prakapenka, V. B., Kubo, A., Kuznetsov, A., Laskin, A., Shkurikhin, O., Dera, P., ... & Sutton, S. R. (2008). Advanced flat top laser heating system for high pressure research at GSECARS: application to the melting behavior of germanium. *High Pressure Research*, *28*(3), 225-235.

Prescher, C., & Prakapenka, V. B. (2015). DIOPTAS: a program for reduction of two-dimensional X-ray diffraction data and data exploration. *High Pressure Research*, *35*(3), 223-230.

Rohrbach, A., & Schmidt, M. W. (2011). Redox freezing and melting in the Earth's deep mantle resulting from carbon–iron redox coupling. *Nature*, *472*(7342), 209-212.

Sakamaki, K., Takahashi, E., Nakajima, Y., Nishihara, Y., Funakoshi, K., Suzuki, T., & Fukai, Y. (2009). Melting phase relation of FeH_x up to 20 GPa: Implication for the temperature of the Earth's core. *Physics of the Earth and Planetary Interiors*, *174*(1-4), 192-201.

Schwager, B., Chudinovskikh, L., Gavriliuk, A., & Boehler, R. (2004). Melting curve of H_2O to 90 GPa measured in a laser-heated diamond cell. *Journal of Physics: Condensed Matter*, *16*(14), S1177.

Shim, S. H. (2017). PeakPo - A python software for X-ray diffraction analysis at high pressure and high temperature. *Zenodo*. http://doi.org/10.5281/zenodo.810199

Solomatov, V. S., & Moresi, L. N. (2002). Small-scale convection in the D″ layer. *Journal of Geophysical Research: Solid Earth*, *107*(B1), ETG-3.

Stixrude, L., & Lithgow-Bertelloni, C. (2011). Thermodynamics of mantle minerals-II. Phase equilibria. *Geophysical Journal International*, *184*(3), 1180-1213.

Tagawa, S., Sakamoto, N., Hirose, K., Yokoo, S., Hernlund, J., Ohishi, Y., & Yurimoto, H. (2021). Experimental evidence for hydrogen incorporation into Earth's core. *Nature communications*, *12*(1), 1-8.

Tang, M., Chen, K., & Rudnick, R. L. (2016). Archean upper crust transition from mafic to felsic marks the onset of plate tectonics. *Science*, *351*(6271), 372-375.

Terasaki, H., Ohtani, E., Sakai, T., Kamada, S., Asanuma, H., Shibazaki, Y., ... & Funakoshi, K. I. (2012). Stability of Fe–Ni hydride after the reaction between Fe–Ni alloy and hydrous phase (δ-AlOOH) up to 1.2 Mbar: Possibility of H contribution to the core density deficit. *Physics of the Earth and Planetary Interiors*, *194*, 18-24.

Thompson, E. C., Davis, A. H., Bi, W., Zhao, J., Alp, E. E., Zhang, D., ... & Campbell, A. J. (2018). High-pressure geophysical properties of Fcc phase FeH_x. *Geochemistry, Geophysics, Geosystems*, *19*(1), 305-314.

Umemoto, K., & Hirose, K. (2015). Liquid iron-hydrogen alloys at outer core conditions by first-principles calculations. *Geophysical Research Letters*, *42*(18), 7513-7520.

Walter, M. J. (2021). Water transport to the core–mantle boundary. *National Science Review*, *8*(4), nwab007.

Wang, X., Scandolo, S., & Car, R. (2005). Carbon phase diagram from ab initio molecular dynamics. *Physical review letters*, *95*(18), 185701.

Wänke, H. (1981). Constitution of terrestrial planets. *Philosophical Transactions of the Royal Society of London. Series A, Mathematical and Physical Sciences*, *303*(1477), 287-302.

Wirth, R., Dobrzhinetskaya, L., Harte, B., Schreiber, A., & Green, H. W. (2014). High-Fe (Mg,Fe)O inclusion in diamond apparently from the lowermost mantle. *Earth and Planetary Science Letters*, *404*, 365-375.

Wood, B. J., Li, J., & Shahar, A. (2013). Carbon in the core: its influence on the properties of core and mantle. *Reviews in Mineralogy and Geochemistry*, *75*(1), 231-250.

Yu, S., & Garnero, E. J. (2018). Ultralow velocity zone locations: A global assessment. *Geochemistry, Geophysics, Geosystems*, *19*(2), 396-414.

Yuan, L., Ohtani, E., Ikuta, D., Kamada, S., Tsuchiya, J., Naohisa, H., ... & Suzuki, A. (2018). Chemical reactions between Fe and H_2O up to megabar pressures and implications for water storage in the Earth's mantle and core. *Geophysical Research Letters*, *45*(3), 1330-1338.

References From the Supporting Information

Fei, H., & Katsura, T. (2020). High water solubility of ringwoodite at mantle transition zone temperature. *Earth and Planetary Science Letters*, *531*, 115987.

Fu, S., Yang, J., Karato, S. I., Vasiliev, A., Presniakov, M. Y., Gavriliuk, A. G., ... & Lin, J. F. (2019). Water concentration in single-crystal (Al, Fe)-bearing bridgmanite grown from the hydrous melt: Implications for dehydration melting at the topmost lower mantle. *Geophysical Research Letters*, *46*(17-18), 10346-10357.

Iwamori, H. (2004). Phase relations of peridotites under H_2O-saturated conditions and ability of subducting plates for transportation of H_2O. *Earth and Planetary Science Letters*, *227*(1-2), 57-71.

van Keken, P. E., Hacker, B. R., Syracuse, E. M., & Abers, G. A. (2011). Subduction factory: 4. Depth-dependent flux of H_2O from subducting slabs worldwide. *Journal of Geophysical Research: Solid Earth*, *116*(B1).

Okamoto, K., & Maruyama, S. (2004). The eclogite–garnetite transformation in the MORB+ H_2O system. *Physics of the Earth and Planetary Interiors*, *146*(1-2), 283-296.

Shieh, S. R., Mao, H. K., Hemley, R. J., & Ming, L. C. (1998). Decomposition of phase D in the lower mantle and the fate of dense hydrous silicates in subducting slabs. *Earth and Planetary Science Letters*, 159(1-2), 13-23.

Geophysical Research Letters

Supporting Information for

Water-induced Diamond Formation at Earth's Core-Mantle Boundary

Byeongkwan Ko[1*], Stella Chariton[2], Vitali Prakapenka[2], Bin Chen[3], Edward J. Garnero[1], Mingming Li[1], Sang-Heon Shim[1]

[1]School of Earth and Space Exploration, Arizona State University, Tempe, AZ, USA
[2]Center for Advanced Radiation Sources, University of Chicago, Chicago, IL, USA
[3]Hawaii Institute of Geophysics and Planetology, University of Hawaii at Manoa, Honolulu, HI, USA

[*]Now at Department of Earth and Environmental Sciences, Michigan State University, East Lansing, MI, USA

Corresponding author: Byeongkwan Ko (kobyeong@msu.edu)

Contents of this file

Introduction

This supporting information provides the supplementary texts and figures to support the main article.

Text S1. X-ray diffraction patterns after temperature-quench at high pressures

After temperature-quench, X-ray diffraction (XRD) patterns show many more peaks. In some patterns, diffraction lines of py-$FeOOH_x$ and fcc-FeH_x remain upon the temperature-quench. However, there were many more lines and they were difficult to interpret. In some patterns, we observed ϵ-$FeOOH_x$ instead of the pyrite-type FeOOH with additional diffraction lines which could not be interpreted. It is possible that a range of temperatures during quench process could have resulted in formation of metastable phases in Fe-O-H-C. We conjecture that the unassigned peaks may come from iron hydride phase (dhcp-FeH_x, FeH_2, or FeH_3) and iron oxide phase (η-Fe_2O_3 or Fe_2O_3 in post-perovskite structure). However, the assignments for these metastable phases remain inconclusive.

Test S2. Estimation of chemical exchange between the mantle and the core

The number of moles of H_2O required to form a mole of C, $NR(\mathrm{H_2O/C})$, through the reaction between water and the core can be calculated from:

$$NR(\mathrm{H_2O/C}) = R(\mathrm{H_2O/Fe})\frac{N_{\mathrm{core}}(\mathrm{Fe})}{N_{\mathrm{core}}(\mathrm{C})},$$

where $R(\mathrm{H_2O/Fe})$ is the molar ratio of H_2O/Fe in the reaction, and $N(\mathrm{Fe})_{\mathrm{core}}$ and $N(\mathrm{C})_{\mathrm{core}}$ are the moles of Fe and C in the core, respectively. We assumed $R(\mathrm{H_2O/Fe}) = 1/3$ (a mole of H_2O reacts with 3 moles of Fe) based on the reaction 3Fe + H_2O = 2FeH + FeO. Then, the equation above can be rewritten as follows:

$$NR(\mathrm{H_2O/C}) = R(\mathrm{H_2O/Fe})\frac{X_{\mathrm{core}}(\mathrm{Fe})\cdot M_{\mathrm{core}}}{m(\mathrm{Fe})}\frac{m(\mathrm{C})}{X_{\mathrm{core}}(\mathrm{C})\cdot M_{\mathrm{core}}}$$

where $m(\mathrm{C})$ and $m(\mathrm{Fe})$ are the molar masses of C and Fe, respectively. $X_{\mathrm{core}}(\mathrm{C})$ and $X_{\mathrm{core}}(\mathrm{Fe})$ are the weight fraction of C and Fe in the core, respectively. M_{core} is the mass of the core. For $X_{\mathrm{core}}(\mathrm{C})$, we used 0.9–2.0 wt% for the carbon content in the outer core (Nakajima et al., 2015; Li et al., 2019). For $X_{\mathrm{core}}(\mathrm{Fe})$, 80 wt% was assumed. Using the obtained $NR(\mathrm{H_2O/C})$=2.9–6.4, an annual carbon transfer from the core to the mantle $F_{\mathrm{CMB}}(\mathrm{C})$ can be estimated from:

$$F_{\mathrm{CMB}}(\mathrm{C}) = m(\mathrm{C})\frac{f(\mathrm{H_2O})\cdot F_{\mathrm{surface}}(\mathrm{H_2O})}{NR(\mathrm{H_2O/C})}$$

where $F_{\mathrm{surface}}(\mathrm{H_2O})$ is the global present-day water flux via subduction into the interior (3×10^{12} kg/yr or 1.7×10^{14} moles/yr; Cai et al., 2018) and $f(\mathrm{H_2O})$ is the water amount reacting with the core at the CMB divided by the water amount subducted at the surface (0–1; we call efficiency term). We obtained $F_{\mathrm{CMB}}(\mathrm{C})$=0.09–2.1 x 10^{11} kg/yr C for the efficiency of 0.03–0.3 (i.e., 3-30%). Assuming constant water transport to the CMB since subduction initiated (2.5–3.5 Ga; Laurent et al., 2014; Tang et al., 2016; Condie and Kröner, 2008) and that the released carbon remains in the mantle, the total carbon amount added to the mantle $\Delta X_{\mathrm{mantle}}(\mathrm{C})$ for the time interval Δt=3 Ga can be calculated in weight fraction:

$$\Delta X_{\text{mantle}}(\text{C}) = \int_0^{\Delta t} \frac{F_{\text{CMB}}(\text{C})}{M_{\text{mantle}}} dt \approx \frac{\Delta t \cdot F_{\text{CMB}}(\text{C})}{M_{\text{mantle}}}$$

where M_{mantle} is the mass of the mantle. We note that time-dependent changes for the terms are assumed to be constant as they are not well known. For example, $F_{\text{surface}}(\text{H}_2\text{O})$ and $f(\text{H}_2\text{O})$ would be sensitive to mantle temperature which might have been higher in the past. The results are illustrated in Fig. 2B.

We also estimated the amount of hydrogen incorporated in the core through the water-induced reaction at the CMB. All hydrogen atoms are assumed to alloy with Fe with a 1:1 ratio and be incorporated in the liquid outer core. Therefore, 2 moles of FeH form from a mole of H_2O $R(\text{FeH/H}_2\text{O}) = 2$. Then, an annual addition of hydrogen to the core can be expressed as follows:

$$F_{\text{CMB}}(\text{H}) = m(\text{H}) \cdot R(\text{FeH/H}_2\text{O}) \cdot f(\text{H}_2\text{O}) \cdot F_{\text{surface}}(\text{H}_2\text{O})$$

where $m(\text{H})$ is the molar mass of hydrogen. Assuming constant water transport to the CMB since initiation of subduction, $\Delta t = 3$ Ga, and that the incorporated hydrogen remains in the core, the total hydrogen amount added to the core can be calculated in weight fraction:

$$\Delta X_{\text{core}}(\text{H}) = \int_0^{\Delta t} \frac{F_{\text{CMB}}(\text{H})}{X_{\text{core}}(\text{H}) \cdot M_{\text{core}}} dt \approx \frac{\Delta t \cdot F_{\text{CMB}}(\text{H})}{X_{\text{core}}(\text{H}) \cdot M_{\text{core}}}$$

where $X_{\text{core}}(\text{H})$ is the weight fraction of hydrogen in the present-day outer core (0.3–2.0 wt%; Terasaki et al., 2012; Umemoto and Hirose, 2015; Thompson et al., 2018; Tagawa et al., 2021). The results are illustrated in Fig. 2C.

Text S3. Reaction efficiency of water at the core-mantle boundary

The fraction of water reacting with the core at the CMB relative to the surface water flux into the interior via subduction is highly uncertain. Much of subducted water should be released during its long journey to the CMB. It is likely that most of the water in the crust in subducted slabs is lost in the upper mantle (<300 km depth) because the geotherms of most subducting crusts cross dehydration or melting of hydrous minerals (Okamoto and Maruyama, 2004; Keken et al., 2011). The harzburgitic layer in subducting slabs can still carry a considerable amount of water as its temperature is much cooler than the top layer of subducting slabs (Iwamori, 2004). As a result, only a small fraction of subducted water may be further transported into the deep mantle (e.g., ~32% based on the thermal models of subduction zones from Keken et al., 2011). Hydrous minerals in subducting slabs would undergo another extensive breakdown in the topmost lower mantle (700–800 km depth; Shieh et al., 1998; Nishi et al., 2014).

However, it is possible that a substantial portion of the released water re-hydrates the nominally anhydrous mineral bridgmanite (~0.01 wt% H_2O) (Fu et al., 2019) in the harzburgitic layer or forms hydrous minerals in the crust, such as phase H (Nishi et al., 2014), AlOOH (Piet et al., 2020), FeOOH (Nishi et al., 2017), and hydrous SiO_2 (Nisr et al., 2020). If all the water remained in subducting slabs in the lower mantle was re-hydrated by these hydrous minerals in subducting slabs and eventually participates in the reaction with the outer core at the CMB, the fraction is ~30%. If the re-hydration process only occurs within the harzburgitic layer in the subducting slabs, the amount of water preserved in slabs is limited to the water solubility of bridgmanite (0.01 wt% H_2O), which is one tenth of the water solubility of ringwoodite (~1 wt% H_2O; Fei and Katsura, 2020). This will lower the fraction an order of magnitude, to ~3%, even if all the water at the CMB reacts with the outer core. Quantifying how much water arrives at the CMB is difficult because of large uncertainties in dehydration and re-hydration processes in the mantle (Walter, 2021). We assume 3–30% of subducted water may arrive at the CMB. One should be careful to use our estimation because in reality some amount of the water at the CMB could react with the surrounding lowermost mantle instead of the outer core.

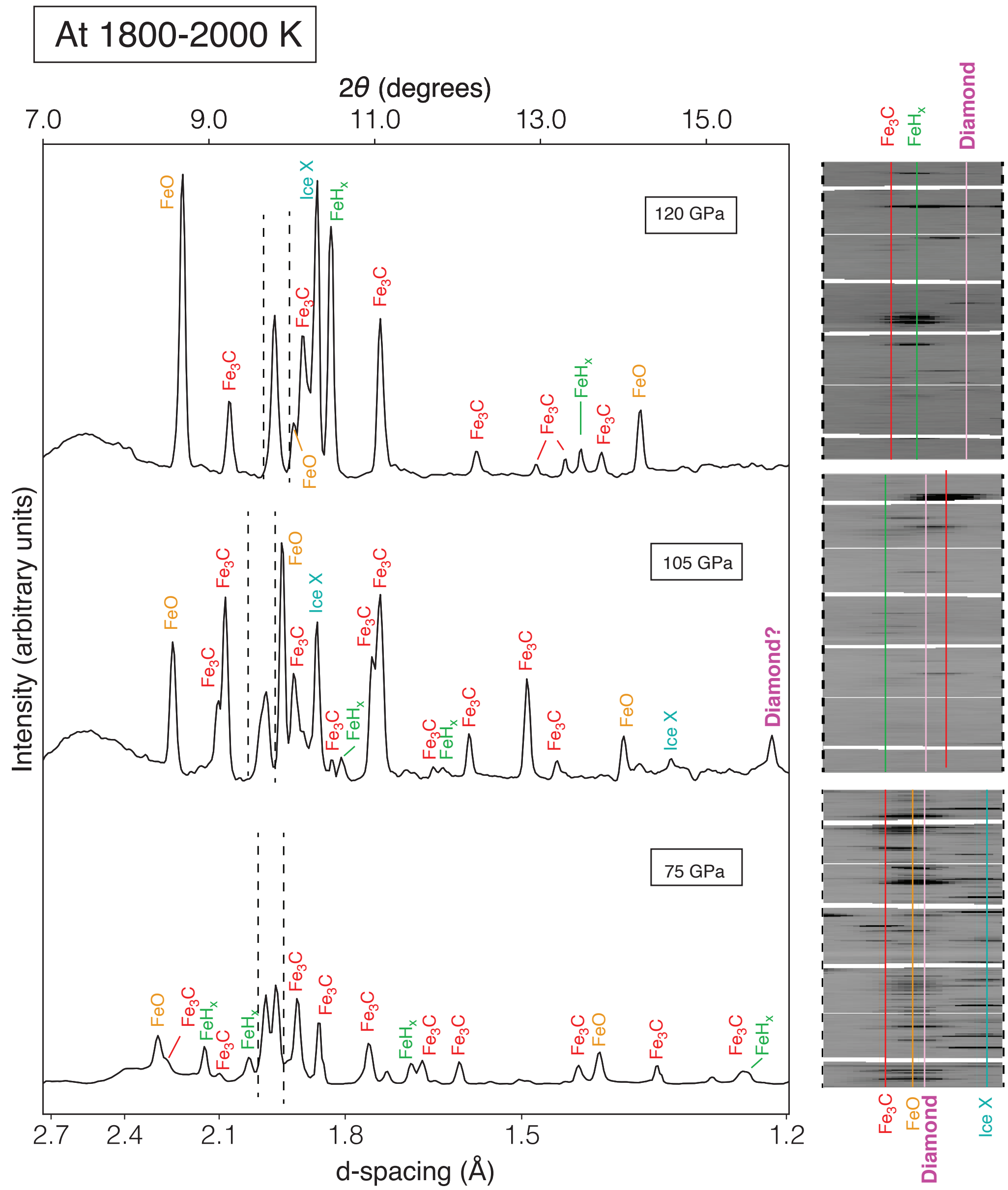

Figure S1 In-situ X-ray diffraction (XRD) patterns of the sample at 75–120 GPa and 1,800–2,000 K in laser-heated diamond anvil cell (LHDAC). X-ray energy was 30 keV. The background is subtracted. The 2-D diffraction images corresponding to the peaks between the dashed lines are shown on the right-hand side. The characteristic line of diamond 111 is observed in the 2-D diffraction images.

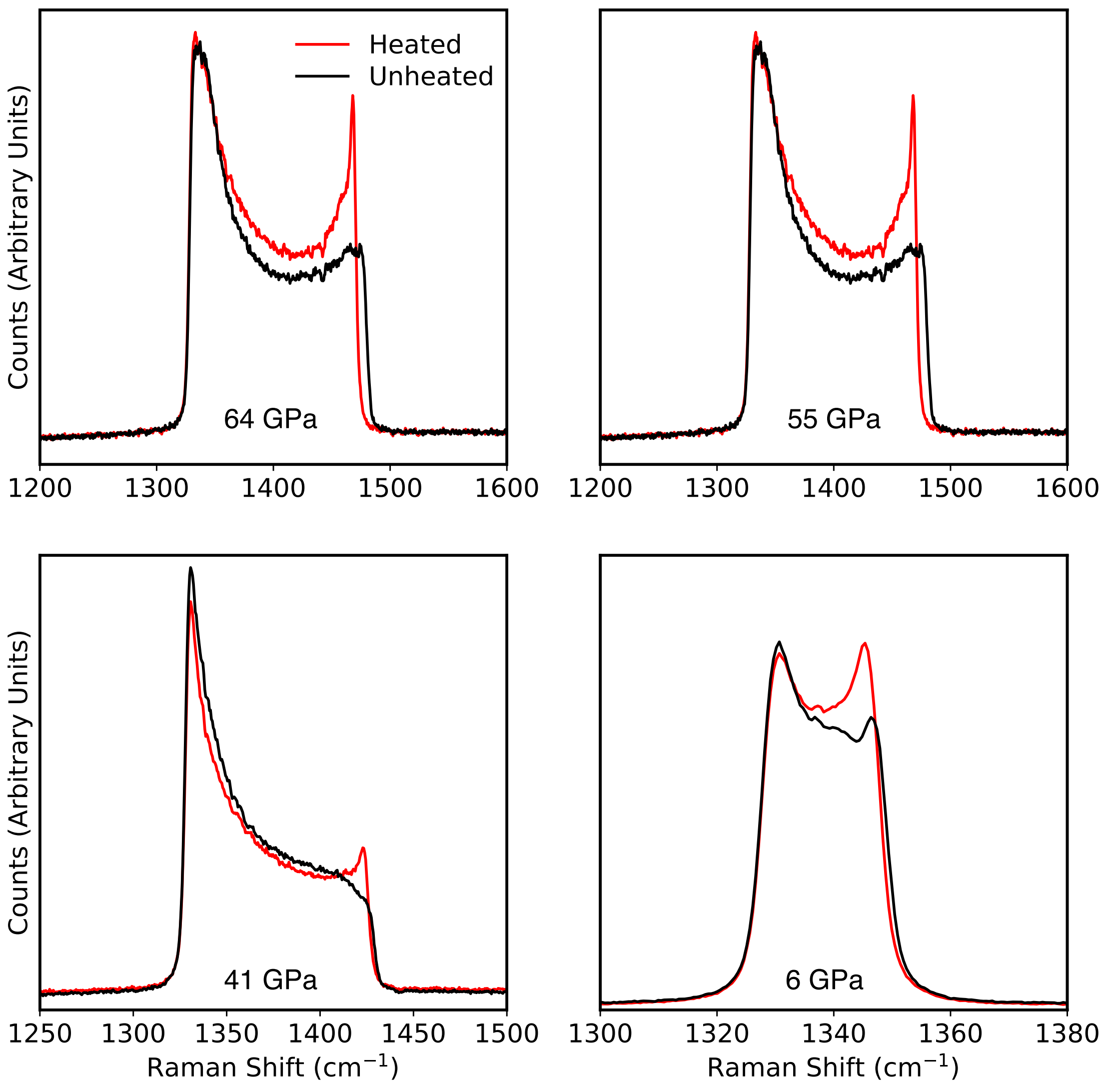

Figure S2 High-pressure Raman spectra of the sample. The sample was synthesized at 71 GPa and 1,800 K. The black spectra were measured at an unheated portion of the sample and the red spectra were measured at the center of heated portion of the sample. The sharp peaks of the red spectra at the edge on the right-hand side are from diamond crystals formed by the reaction between Fe_3C and H_2O.

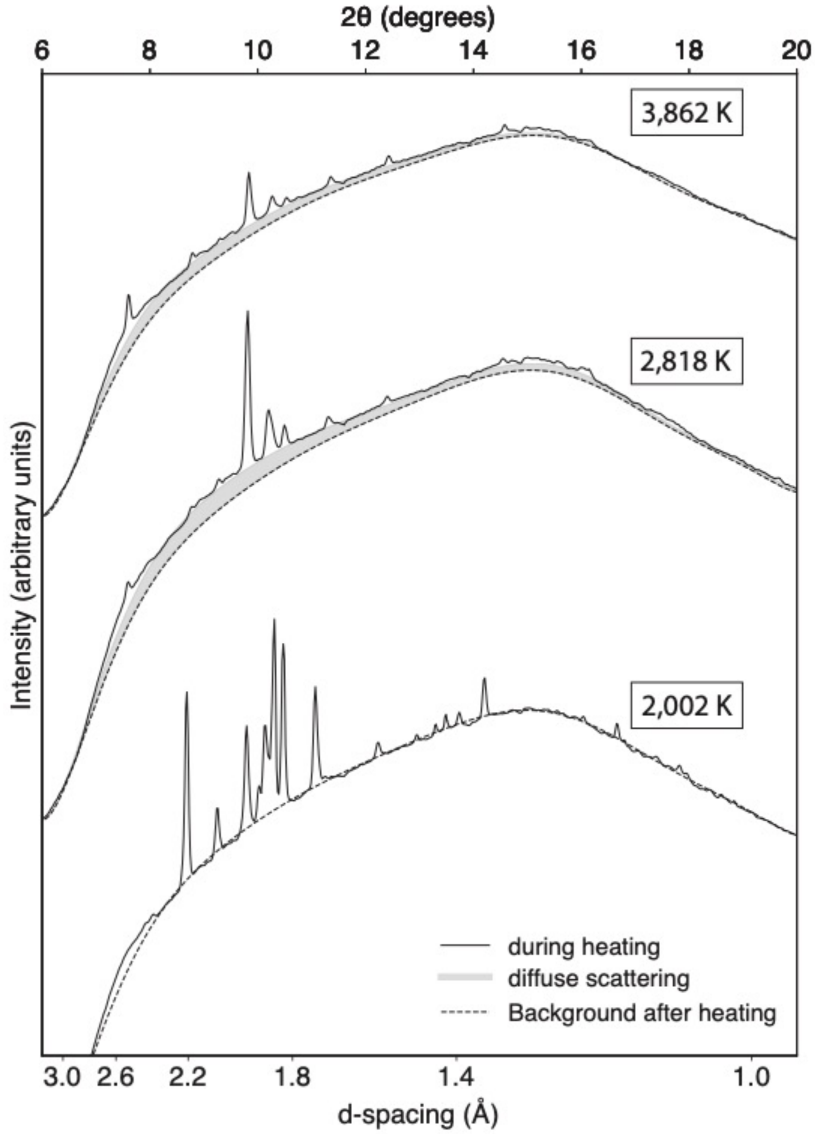

Figure S3 In-situ X-ray diffraction (XRD) patterns of the sample at 120-140 GPa and 2,002–3,862 K in laser-heated diamond anvil cell (LHDAC). X-ray energy was 30 keV. The diffuse scattering at 2,818 and 3,862 K indicates melting occurs at those temperatures at 120-140 GPa.